Infrared lock-in carrierography (photocarrier radiometric imaging) of Si solar cells

A. Melnikov, A. Mandelis,[a] J. Tolev, P. Chen, and S. Huq
Department of Mechanical and Industrial Engineering, Center for Advanced Diffusion-Wave Technologies (CADIFT), University of Toronto, Ontario M5S 3G8, Canada

(Received 18 February 2010; accepted 25 March 2010; published online 9 June 2010)

Modulated photocarrier radiometric (PCR) imaging (lock-in carrierography) of multicrystalline (mc) Si solar cells is introduced using a near-infrared (NIR) InGaAs camera and a spread superband gap laser beam as an optoelectronic source at low modulation frequencies (<10 Hz) or point-by-point scanning PCR imaging with a focused laser beam at high (kilohertz) frequencies. PCR images are supplemented by quantitative PCR frequency scans and compared to NIR optical reflectance, modulated electroluminescence (MEL) and modulated photovoltage (MPV) images. Noncontact PCR imaging is controlled by the photoexcited carrier diffusion wave and exhibits very similar images to contacting MEL and MPV. Among these methods it exhibits the highest contrast and sensitivity to mechanical and crystalline defects in the substrate at lock-in image frequencies in the range of the inverse recombination lifetime in the quasineutral region (bulk). © *2010 American Institute of Physics*. [doi:10.1063/1.3407521]

I. INTRODUCTION

There is considerable fundamental and practical importance attached to developing all-optical, nondestructive and noncontacting diagnostic methodologies for monitoring the energy conversion mechanisms affecting efficiency and transport properties of solar cells as a function of substrate crystal growth and/or device processing steps without the application of electrodes or the need for fully operational insert devices.[1] The method that comes closest to these requirements is room temperature photoluminescence (PL).[2] Among camera-based imaging techniques PL, capturing radiative near-infrared (NIR) emissions in the range of 0.9 to 1.7 μm, as well as midinfrared thermography, capturing thermal infrared emissions in the range of 4 to 20 μm, have been applied successfully for spatial mapping of mechanical defects, carrier lifetime, diffusion length, trap density and dislocation density.[3–8] However, dc PL is spectrally wideband, that is, it only yields depth-integrated spectroscopic information on radiative emission processes from/to various intraband defect states (often a superposition of overlapping processes due to thermal and defect state energy broadening). Its quasistatic (steady state) character cannot provide the kinetics of electronic transport and recombination properties responsible for useful photovoltaic (PV) energy conversion as well as energy dissipation. When applied to solar cells, the depth-integrated character of PL cannot probe optoelectronic carrier kinetics and recombination processes at specific depths below the surface, especially at the critical *p-n* junction depth,[5] a crucial region ripe for optimized solar cell design. As a consequence, dc PL imaging has been used for surface diagnostics and quality control with Si-charge coupled device (CCD) and InGaAs cameras and can detect problems associated with mechanical handling and imperfections (cracks) of raw substrates and solar cell devices,[9] but cannot monitor the optoelectronic kinetics of surface and near-subsurface (junction) regions which are of greatest interest to solar-cell design optimization. Electroluminescence (EL) is akin to PL, as it converts electric fields applied to solar cells through their electrical contacts to infrared radiation emitted by the cell surface.[10] It works for cells and modules in the form of CCD camera imaging but requires finished, operational solar cells and does not work with substrates on partly processed devices.

Photocarrier radiometry (PCR), as a dynamic spectrally-gated form of PL,[11] can yield accurate quantitative information about transport and recombination processes in junction devices like solar cells.[12] Due to the high sensitivity of InGaAs photodetectors (e.g., the Thorlabs model PDA400 with a built-in preamplifier has a noise equivalent power (NEP) figure of $2.9-8.2\times10^{-12}$ W $Hz^{-1/2}$), a distinct advantage of PCR over conventional dc and ac PL studies,[13,14] is its ability for *low-intensity operation* in the subquadratic optical excitation regime (signal versus light intensity). PCR, as a band-to-impurity or band-to-defect radiative recombination methodology, is *complementary* to band-to-band recombination PL techniques[14,15] and is thus significantly more sensitive to subband-gap recombination. Furthermore, compared to the recombination superposition character of conventional dc PL, especially at room temperature, PCR offers recombination specificity (kinetic resolution) through labeling various recombination processes with their respective lifetimes.[11,12] Lock-in signal processing combined with superior detector NEP in PCR features considerably higher signal dynamic range than dc PL or PL spectroscopy, thereby requiring much lower illumination intensity, an advantage which solves the well-known problem of optical flooding and/or masking the presence of defect states which act as radiative recombination centers. As a result, PCR can operate in the linear response regime which yields undistorted information on trans-

[a]Electronic mail: mandelis@mie.utoronto.ca.

 © 2010 American Institute of Physics

Downloaded 24 Dec 2010 to 128.100.48.213. Redistribution subject to AIP license or copyright; see http://jap.aip.org/about/rights_and_permissions

port properties,[16] unlike modulated PL using high laser intensities.[14,15]

Advantages of using modulated (lock-in) camera imaging include significant reduction in measurement time and spatial resolution improvement, opening the possibility for dynamic transport property mapping and depth-profilometric images of improved contrast over their dc counterparts. Although lock-in thermography has been used with solar cells, PL and EL camera imaging are performed under dc conditions, to our best knowledge. Furthermore, lock-in imaging has two different channels, amplitude and phase, thus allowing complementary information about material and device parameters and processes. In this paper, we introduce lock-in PCR imaging (carrierography) of mc Si solar cells using both a fast NIR InGaAs camera synchronized with a modulated superband-gap laser beam and a scanned point-by-point superband-gap laser beam PCR method to generate optoelectronic images at low and high modulation frequencies, respectively. In future, we expect to speed up the frame rate of our camera so as not to have to rely on point-by-point carrierographic imaging at high frequencies (>100 Hz). The carrierographic images are supplemented by optical reflectivity, modulated EL (MEL), modulated photovoltage (MPV) images, and conventional PCR and MPV frequency scans in order to enhance our understanding of the physical origins of the images and assist the interpretation of image contrast.

II. MATERIALS AND EXPERIMENTAL

A solar cell featuring a *p-n* junction fabricated on a *p*-type industrial mc Si wafer (156×156 mm^2 area, 200 μm thickness from Enfoton, Cyprus) was used for measurements. A substrate Si wafer and another solar cell (a fragment with electrodes) were subjected to mechanical damage. The experimental imaging system contains a high-speed near infrared InGaAs camera (SU320KTSW-1.7RT/RS170 from Goodrich Sensors Unlimited) with a 320×256 pixel active element, spectral bandwidth 0.9–1.7 μm, noise equivalent irradiance $<2.5\times10^9$ photons/cm^2 s, and maximum frame-rate 119 fps for 320×256 window size and 11700 fps for 16×16 window size. A schematic of the system is shown in Fig. 1(a).

For lock-in carrierographic camera imaging at low frequencies, a 532-nm solid-state laser (Coherent, model Verdi V-10) in combination with an acousto-optic modulator delivered sinusoidally modulated radiation. The laser beam size for area imaging was about 2 cm and maximum frequency was set at 10 Hz. This upper limit was imposed by the maximum full-frame rate of the camera so as to allow for fourfold oversampling the PCR images collected at each modulation period, thus enabling a high SNR construction and storage of lock-in in-phase (IP) and quadrature (Q) images above the conventional twofold oversampling rate used in lock-in thermography[17] with computer-generated amplitude and phase images derived from the IP and Q images. The camera images were read by the computer using a PCI-1427 frame grabber from National Instruments to produce computer-generated amplitude and phase images. Using a smaller 160×128 pixel window size, a maximum laser modulation frequency of 100 Hz has been achieved. With the current software, further decreases in the size of the frame produce amplitude and phase images with little contrast. For producing modulated (lock-in) MEL imaging (MELI), a voltage power supply was used with the same InGaAs camera and lock-in imaging software developed for lock-in carrierography. NIR optical reflectivity images of the laser illuminated areas were obtained using a halogen light source (150 W, Navitar 150 Illuminator).

PCR frequency scans are known to yield information about optoelectronic transport properties of semiconductor materials and devices[11] which ultimately control the contrast in IR lock-in carrierography, depending on the modulation frequency. Therefore, for the interpretation of our images, frequency scans were performed from 10 Hz to 100 kHz at room temperature in the dark, so as not to add background photovoltage (dc optical bias) which can alter the frequency response of solar cells. The experimental PCR configuration with a focused current-modulated semiconductor laser is shown in Fig. 1(b). The laser wavelength and average spot-size on the solar cell were 830 nm and 110 μm, respectively. The PCR signal from near-infrared radiative emissions from the solar cell was detected using a single InGaAs diode detector PDA400 with spectral bandwidth 0.7–1.8 μm and frequency response up to 10 MHz. The PCR and MPV signals were measured simultaneously using two lock-in amplifiers. A long-pass filter LP-1000 nm from Spectrogon with $>70\%$ transmission for spectral range 1000–2200 nm was used to block the excitation laser beam from the detector and InGaAs camera. For point-by-point imaging scans the solar cell was irradiated with a square-wave-modulated laser beam at fixed modulation frequency leading to high-frequency PCR images, or at fixed coordinate points leading to single-point PCR frequency scans. MPV imaging (MPVI) was also achieved using the same point-by-point scans and recording the photovoltage at each coordinate point. An additional 980-nm secondary laser was used along with the 830-nm laser in some experiments in which one of the two beams was acting as dc optical bias.

III. RESULTS AND DISCUSSION

A. Si wafer imaging

The PCR signal from optoelectronic semiconductors, and Si in particular, depends mainly on diffusing minority carrier-wave recombination lifetimes, the ambipolar diffusion coefficient, and front and back surface recombination velocities.[11] To ensure proper functionality of the lock-in carrierography system, our earlier single-point PCR area-scanned experiments with damaged Si wafer back-surfaces[11,18] were revisited, this time using the InGaAs camera. The purpose of these experiments was to show the sensitivity of PCR imaging to the boundary conditions at the back-surface of the wafer and their diminished importance as contrast mechanism with increasing frequency (decreasing carrier density-wave wavelength), thereby proving the depth profilometric nature of IR carrierography. The surface of

Downloaded 24 Dec 2010 to 128.100.48.213. Redistribution subject to AIP license or copyright; see http://jap.aip.org/about/rights_and_permissions

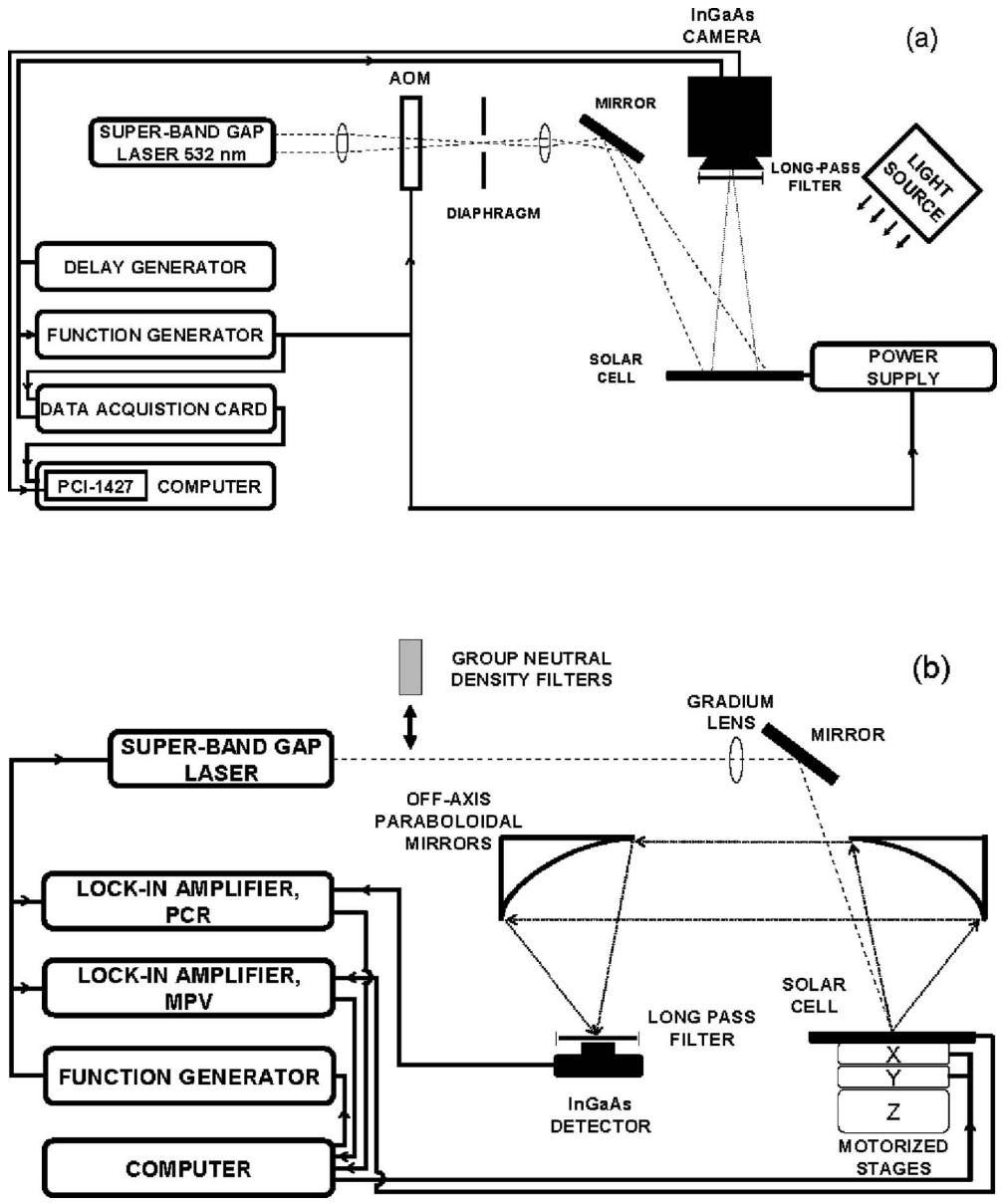

FIG. 1. (a) Infrared lock-in carrierographic and EL (dc and modulated) imaging setup for dynamic solar-cell optoelectronic diagnostic imaging. (b) Experimental setup for MPV and PCR with focused laser beam and a single-element InGaAs photodiode.

a small area of a Si wafer back-side was mechanically damaged through gentle rubbing with fine sandpaper. Figure 2 shows the lock-in carrierographic image amplitude of this and the adjacent intact area obtained with the camera at 10 Hz. Although the optical absorption depth at the excitation wavelength is very short (a few micrometers), the image clearly reveals the damaged area 700 μm deep through the recombinations of the photoexcited free-carrier density wave.[19] The phase image was also obtained but is not shown here because the PCR phase contrast is poor at low frequencies. The centroid of the free-carrier-wave density integral[11]

$$S(\omega) \approx F(\lambda_1,\lambda_2)\int_0^L \Delta N(z,\omega)dz \tag{1}$$

consists of contributions from radiative recombinations in the bulk and at the front surface, whereas enhanced nonradiative recombination at, and decreased radiative emissions from, the damaged back surface create imaging contrast (dark area), provided the frequency is low enough for the ac carrier diffusion length[19]

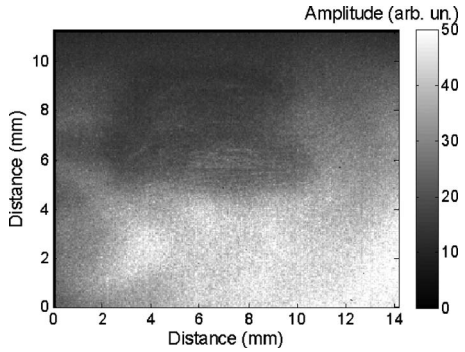

FIG. 2. Lock-in carrierographic amplitude image of a Si wafer with localized mechanical back-side damage. The boundary with the undamaged area is clearly visible. Frequency: 10 Hz.

Downloaded 24 Dec 2010 to 128.100.48.213. Redistribution subject to AIP license or copyright; see http://jap.aip.org/about/rights_and_permissions

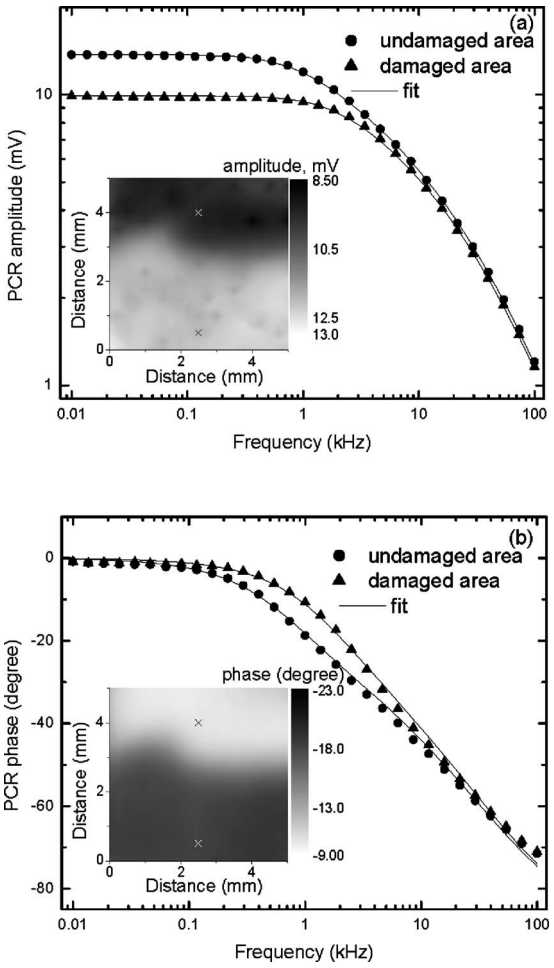

FIG. 3. PCR frequency dependencies obtained from the front-surface of the silicon wafer of Fig. 1 with the laser beam over the intact and the partially damaged back surface as shown in the inset images. Images were constructed from point-by-point focused laser scans with 250 μm step at 1 kHz and spotsize ~110 μm. (a) Amplitude and (b) phase. **x** indicates the frequency scan location. Symbols: experimental data; lines: theoretical best fits.

$$L_e(\omega) = \sqrt{\frac{D^*\tau}{1+i\omega\tau}} \tag{2}$$

to be large, or on the order of, the wafer thickness, L.[11,20] In Eqs. (1) and (2), F is a function of the spectral bandwidth (λ_1,λ_2) of the IR detector; $\Delta N(z,\omega)$ is the optically generated excess free-carrier-wave density at depth z; D^* is the ambipolar carrier diffusivity and τ is the minority recombination lifetime. PCR frequency scans from the front-surface over the damaged and undamaged back-side are shown in Fig. 3. The best fitted data according to the three-dimensional PCR model[11] are presented in Table I. The mechanical damage on the back side has led to significant reduction in carrier recombination lifetimes and increase in backside recombination velocities. The imaging frequency was chosen to be 1 kHz to yield optimum contrast for both amplitude and phase, guided by the frequency scans in the neighborhood of the "knee." It is clear that the physical origin and contrast of both camera and point-by-point images are due to variations in modulated photocarrier density (photocarrier wave), whence the motivation for naming the NIR camera based technique "lock-in carrierography."

B. Si solar-cell imaging

1. Low-frequency lock-in EL and carrierographic camera images

The NIR optical image of a 1.41×1.13 cm^2 area of the commercial mc silicon solar cell (illuminated with a halogen lamp and imaged with the same InGaAs camera operating in the dc mode) is shown in Fig. 4(a). In the wavelength range 1.0–1.7 μm, silicon is mainly transparent, therefore, the image is generated by reflected light from front and back surfaces and grain boundaries. The vertical equidistant bars belong to the current capturing electrode grid. Texturing etching during solar cell fabrication contributes to image contrast at the upper-left corner of the image which shows dislocation clustering and various surface defects. Single-crystalline grains of various sizes and orientations are visible. A dc EL image of the same solar cell area was obtained with the application of 633 mV across the solar cell electrodes and is shown in Fig. 4(b). As reported earlier,[3] the EL intensity distribution is linked to the distribution of minority carrier dc diffusion length in the active layer

$$L_{\rm dc} = \sqrt{D^*\tau}. \tag{3}$$

Low diffusion-length areas are associated with high concentration of small grains, the latter acting as enhanced nonradiative recombination centers. Lock-in EL images were further obtained upon application of sinusoidally modulated voltage in the forward bias mode across the solar cell. The amplitude image is shown in Fig. 4(c). It exhibits the same spatial features as the dc EL image, as expected from the condition $\omega\tau \ll 1$ which yields $L_e = L_{\rm dc}$. The phase image at 10 Hz is not reported here as it showed minimal contrast, a result of the long diffusion length dominated by bulk recombination and not by grain-boundary optoelectronic processes. However, it is interesting to note that the EL intensity near and along the electrodes is higher. Photon emission damping away from the electrodes is caused by the series resistance in the upper (n-type) layer which decreases the local externally

TABLE I. Fitted parameters of Si wafer with undamaged and damaged back-surface according to the three-dimensional PCR model (Ref. 11).

Transport property	Undamaged back-side area	Damaged back-side area
Lifetime, ms	0.31	0.11
Diffusivity, cm^2/s	2.7	2.7
Front-surface velocity, cm/s	0.0052	0.0068
Back-surface velocity, cm/s	800	1598

Downloaded 24 Dec 2010 to 128.100.48.213. Redistribution subject to AIP license or copyright; see http://jap.aip.org/about/rights_and_permissions

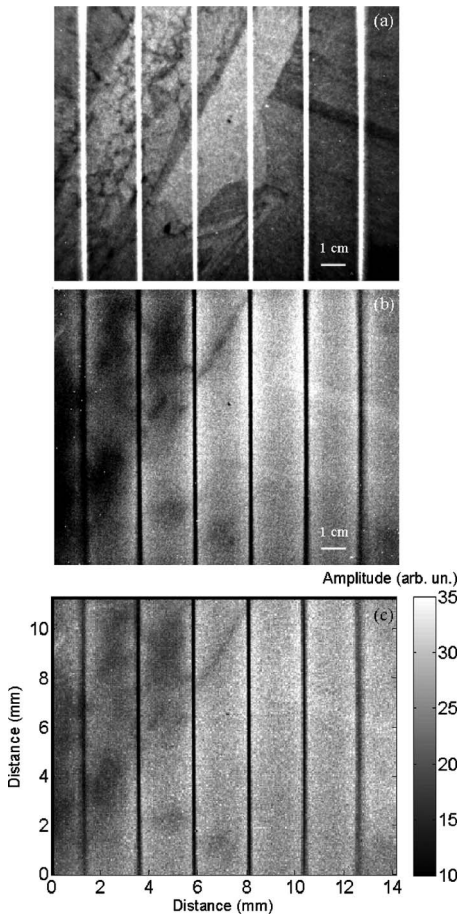

FIG. 4. (a) NIR optical reflection image from an area of a polycrystalline Si solar cell under halogen lamp illumination. (b) dc EL image of the same area under forward bias with applied V=633 mV and 6.3 A. (c) Modulated (lock-in) EL image amplitude of the same area at 10 Hz. All images were obtained with the InGaAs camera.

applied effective forward-bias electric field across the *p-n* junction with distance from the electrode.

The lock-in carrierography image of the same solar-cell area with the modulated 532 nm laser beam at 10 Hz is shown in Fig. 5 (amplitude). Similar features to those present in the EL image appear. The phase image at 10 Hz exhibited poor contrast and is not shown here. The presence of nonradiative recombination centers on the upper left region of the

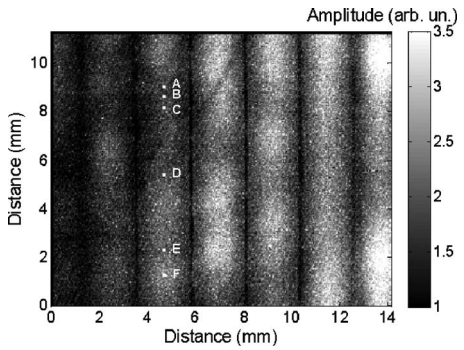

FIG. 5. Lock-in carrierographic amplitude image of the solar-cell area depicted in Fig. 4. Photoexcitation of carriers was induced with the 532-nm laser beam modulated at 10 Hz. The lock-in image was obtained with the InGaAs camera. Points A–F indicate PCR frequency measurement locations (Fig. 6).

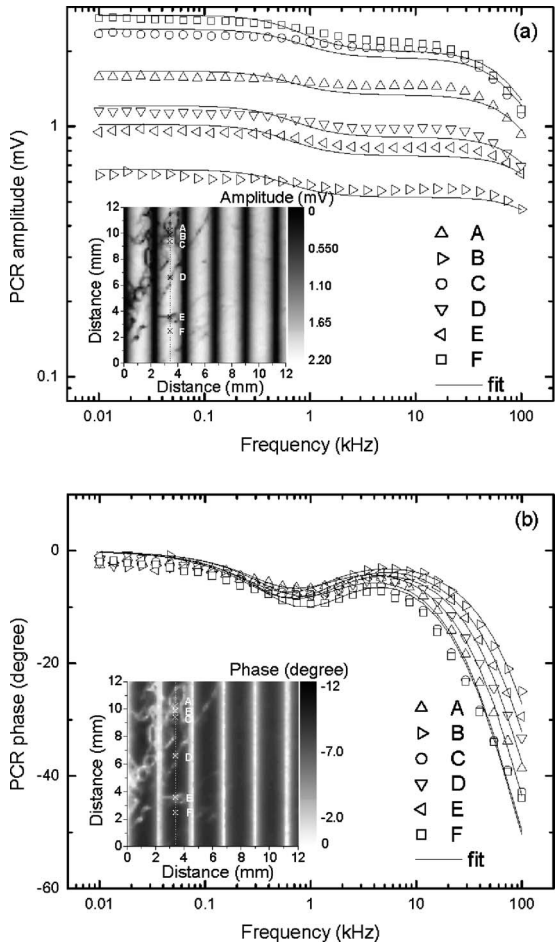

FIG. 6. PCR frequency scan at specific solar cell locations. (a) Amplitude and (b) phase. Inset: 10 kHz point-by-point scanned image with 200 μm step. Laser beam spotsize ~110 μm across the same area in Fig. 5. A–F: coordinates of specific points corresponding to inset image. Symbols: experimental data; lines: theoretical best fits to Eq. (4).

images in Fig. 4 is also corroborated in this image with dark contrast indicative of compromised radiative recombination and low free-carrier density. However, the major advantage of the carrierographic image is its noncontact nature. Unlike the EL images, the regions adjacent to, and along, the electrodes appear darker because the presence of the electrode acts as a drain of excess photocarriers which are exported into the external circuit rather than recombine radiatively locally and emit NIR photons. Indeed, the image brightness is highest at mid-distance between adjacent electrodes where carrier densities are expected to be highest. This is opposite to the modulated EL image of Fig. 4(c).

2. PCR and MPV focused laser-scan imaging and frequency responses

In order to interpret the contrast mechanism(s) of the carrierographic and photovoltage images, PCR frequency scans and the simultaneously measured ac photovoltage frequency scans with high-intensity modulated laser beam (peak power 30.9 mW) from the same area of the solar cell are presented in Figs. 6 and 7, respectively. Points were chosen at mid-distance between electrodes to minimize the effect of series resistance and electrode carrier drain. Full

Downloaded 24 Dec 2010 to 128.100.48.213. Redistribution subject to AIP license or copyright; see http://jap.aip.org/about/rights_and_permissions

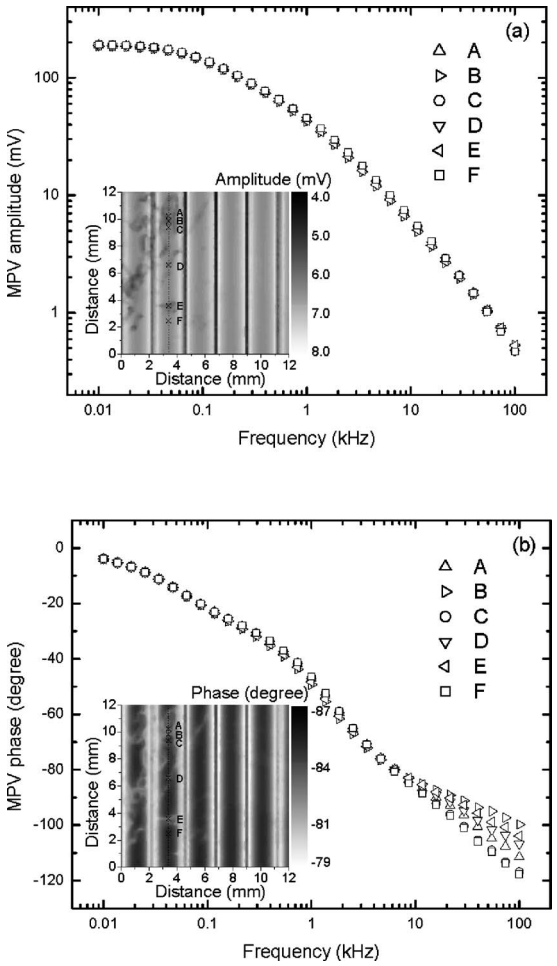

FIG. 7. ac photovoltage (MPV) frequency scan at specific solar cell points locations. (a) Amplitude and (b) phase. Inset: 10 kHz point-by-point scanned image with 200 μm step. Laser beam spotsize ~110 μm across the same area of the solar cell as in Figs. 5 and 6. A–F: coordinates of specific points corresponding to inset image.

point-by-point scanned images are shown in the insets of Figs. 6 and 7. In Fig. 6, all PCR amplitude-frequency responses have two pronounced bending points (knees) with corresponding features in the phase-frequency responses. As was shown earlier, this type of behavior is the result of two time constants. The longer lifetime, τ_1, corresponds to the resistance-capacitance (RC) time constant of the *p-n* junction, while the shorter lifetime, τ_2, corresponds to minority carrier recombination.[12,21] The τ_1 is controlled by junction capacitance and dynamic junction resistance at peak photovoltage. Based on the detailed formulation of the free-carrier-wave problem on both sides of the *p-n* junction[22,23] involving two characteristic lifetimes, the PRC frequency curves were best-fitted to a simplified version of the model[22]

$$S_{\mathrm{PCR}}(f) = \frac{K_1\tau_1}{1+i2\pi f\tau_1} + \frac{K_2\tau_2}{1+i2\pi f\tau_2}, \tag{4}$$

where K_1 and K_2 are material-property-dependent constants. The best-fitted τ_1 and τ_2 values at locations A–F (Fig. 6, inset) are presented in Table II. The results clearly show a decrease in minority carrier lifetime τ_2 in the area with decreased carrierographic amplitude image, Figs. 5 and 6 (inset). The time constant τ_1 changes only slightly as expected

TABLE II. Fitted characteristic lifetimes of mc solar cell at various locations according to two-lifetime PCR model, Eq. (4).

Location	τ_1 (ms)	τ_2 (μs)
A	0.261	1.51
B	0.302	0.81
C	0.224	1.87
D	0.265	1.22
E	0.292	1.00
F	0.227	1.91

from the essentially uniform junction geometry, also accompanied by negligible change in peak photovoltage generated by the modulated laser beam. In a manner similar to the Si wafer carrierographic images of Fig. 3, the optimal contrast in both amplitude and phase images of Fig. 6 is obtained at frequencies around the first and second knees. The point-by-point PCR images at 10 kHz shown in the inset of Fig. 6 correlate very well with features evident in the EL images of Fig. 4 and in the low-frequency lock-in carrierographic image of Fig. 5. The resolution of the images in Fig. 6 is superior to that of the foregoing images owing to the short carrier wavelength (and ac diffusion length) at high frequency. In view of this result, efforts are currently expended to significantly increase the modulation frequency of camera-based lock-in carrierography in order to improve spatial resolution and fast imaging consistent with in-line process monitoring.

Unlike the PCR frequency dependence, the MPV frequency response is significantly less sensitive to the spatial distribution of the transport parameters and nonradiative recombination centers in the solar cell (Fig. 7). The ac photovoltage is slightly higher in areas with longer carrier recombination lifetime, which generates contrast in the MPV image insets very similar to the PCR images in Fig. 6. As with the PCR frequency dependencies, the MPV response in Fig. 7 exhibits two very mild knees, more so in phase than in amplitude. These features are caused by changes in the RC time constant, corresponding to variations in junction resistance and capacitance which change with the photovoltage across the junction under high laser intensity.[12,21] The MPV curves from the various locations A–F are very similar, unlike the PCR frequency scans, with major differences only in the $f > 10$ kHz phase. These differences are related to the short carrier diffusion length at high f being more sensitive to local (near surface) carrier trapping effects which render the phase lags at the locations with high trap densities (e.g., in the form of grain boundaries) smaller than those from nondefective or nonboundary regions. In Fig. 7(b), the order of phase lag increase for $f > 10$ kHz signifies increase in the local optoelectronic quality of the probed site.

In order to study the effects of dc optical bias on the solar cells, MPV frequency scans with low-intensity modulated laser beams at two superband-gap wavelengths from locations near points E and F, Fig. 5, are shown in Fig. 8. 830-nm and 980-nm modulated laser beams were used, as well as a combination of the 980-nm modulated laser beam with a superposed 830-nm dc laser beam (30.9 mW) acting as optical (equivalent forward) bias. Under the superposed

Downloaded 24 Dec 2010 to 128.100.48.213. Redistribution subject to AIP license or copyright; see http://jap.aip.org/about/rights_and_permissions

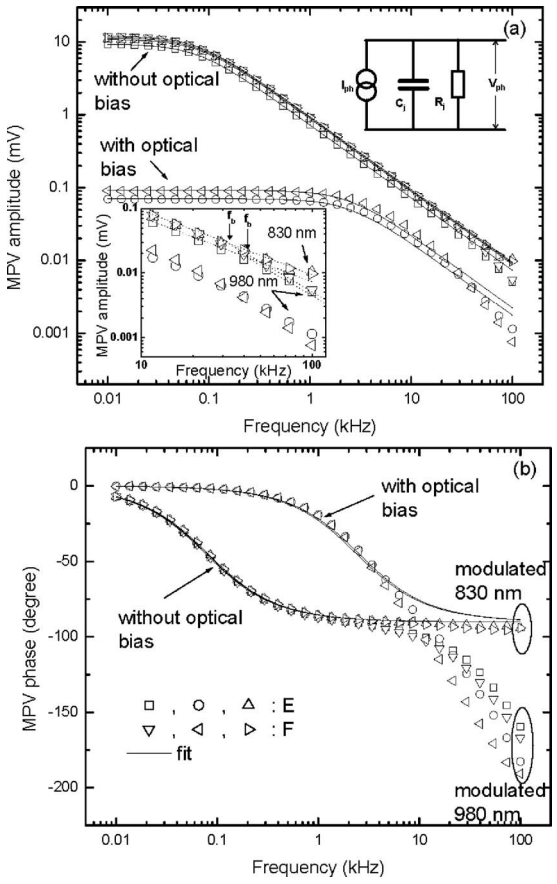

FIG. 8. MPV frequency scan with low-intensity modulated laser beams near points E and F, Fig. 4. (a) amplitude; (b) phase. Point E: □—980-nm modulated beam; ○—980-nm modulated beam, and 830-nm dc beam with the same peak power as in Fig. 7; △—830-nm modulated beam. Point F: ▽—980-nm modulated beam; ◁—980-nm modulated beam and 830-nm dc beam with power equal to the peak power in Fig. 7; ▷—830-nm modulated beam. Theoretical best fits to Eq. (5).

830-nm dc excitation MPV exhibited the same value as the maximum peak photovoltage in the case of the higher power modulated excitation of Fig. 7. The equivalent circuit model in the inset of Fig. 8(a) was used to fit the data to the theoretical photovoltage frequency dependence $V_{ph}(f)$ (Refs. 24 and 25)

$$V_{ph}(f) = I_{ph}\left(\frac{1}{R_j} + i2\pi f C_j\right)^{-1} = \frac{K_3}{1 + i2\pi f \tau_{\mathrm{RC}}}, \qquad (5)$$

where I_{ph} is the photocurrent, $R_j = dV/dI$ is the dynamic junction resistance; C_j is the junction capacitance; f is the modulation frequency; $K_3 = I_{ph}R_j$ is a fitted parameter, and $\tau_{\mathrm{RC}} = R_j C_j$ is the RC time constant. As in the case of the large-amplitude photovoltage from the higher laser power, the small-amplitude MPV is slightly higher at locations with higher carrier recombination lifetime (e.g., point F) for both 830-nm and 980-nm modulated laser beams. The phase frequency dependence is practically the same up to approximately 10 kHz at both locations although it strongly differs for cases with and without optical bias, Fig. 8(b). The knee in the MPV frequency dependence for the *p-n* junction without dc optical bias is in the same frequency range as the first knee in the large-amplitude MPV dependence of Fig. 7. Furthermore, the knee with the 830-nm dc optical (effective forward) bias junction lies in the same range as the second knee in Fig. 7. This correlation confirms that the first knee in the large-amplitude MPV dependence is determined by the RC time constant corresponding to photovoltage near 0 V and the second high-frequency knee is due to the RC time constant corresponding to the peak photovoltage.[12,21] The RC time constants for small-amplitude MPV were derived from fits to Eq. (5) and are presented in Table III. Although they are very different with and without optical bias, however, they are the same at both locations E and F.

We note that in the high frequency range, $f > 10$ kHz, the small-amplitude MPV frequency dependence is different under two-wavelength excitation. For 830 nm modulated excitation, the MPV frequency amplitude follows a f^{-1} dependence and the phase remains practically constant at −90°. For 980 nm modulated excitation, the MPV amplitude deviates from the f^{-1} dependence at higher frequencies (Fig. 8, inset), also followed by significant phase deviations. The appearance of the second knee originates in minority carrier recombination lifetime, when the ac diffusion length becomes shorter than both thickness, L, and optical absorption depth, $1/\alpha$, where α is the optical absorption coefficient.[24,25] Then the minority carrier lifetime can be calculated from $\tau_n = 1/2\pi f_b$, where f_b is the frequency of the knee. The foregoing condition is satisfied for 980-nm high-frequency MPV excitation, for which α is approx. 100 cm^{-1} in silicon. It is important to note that this feature in the MPV frequency dependence is approximately in the same frequency range as the second knee of the PCR frequency dependence. Similar to PCR behavior, the second MPV knee shifts to higher frequencies at locations with smaller carrier recombination lifetimes. The calculated two MPV minority carrier lifetimes from f_b at both locations E and F are also shown in Table III. Some discrepancies in the MPV values (3.8 and 4.8 μs) compared to those obtained from the PCR frequency dependence (1.0 and 1.9 μs) are not well understood at present.

TABLE III. Characteristic lifetimes of mc solar cell at two locations extracted from MPV frequency scan.

	Location E		Location F	
Illumination	τ_{RC} (ms)	τ_n (μs)	τ_{RC} (ms)	τ_n (μs)
Modulated 980-nm laser beam	2.0	3.8	2.1	4.8
Modulated 980-nm laser beam and 30.9 mW 830-nm dc laser beam	0.064		0.066	
830-nm modulated laser beam	2.0		2.0	

Downloaded 24 Dec 2010 to 128.100.48.213. Redistribution subject to AIP license or copyright; see http://jap.aip.org/about/rights_and_permissions

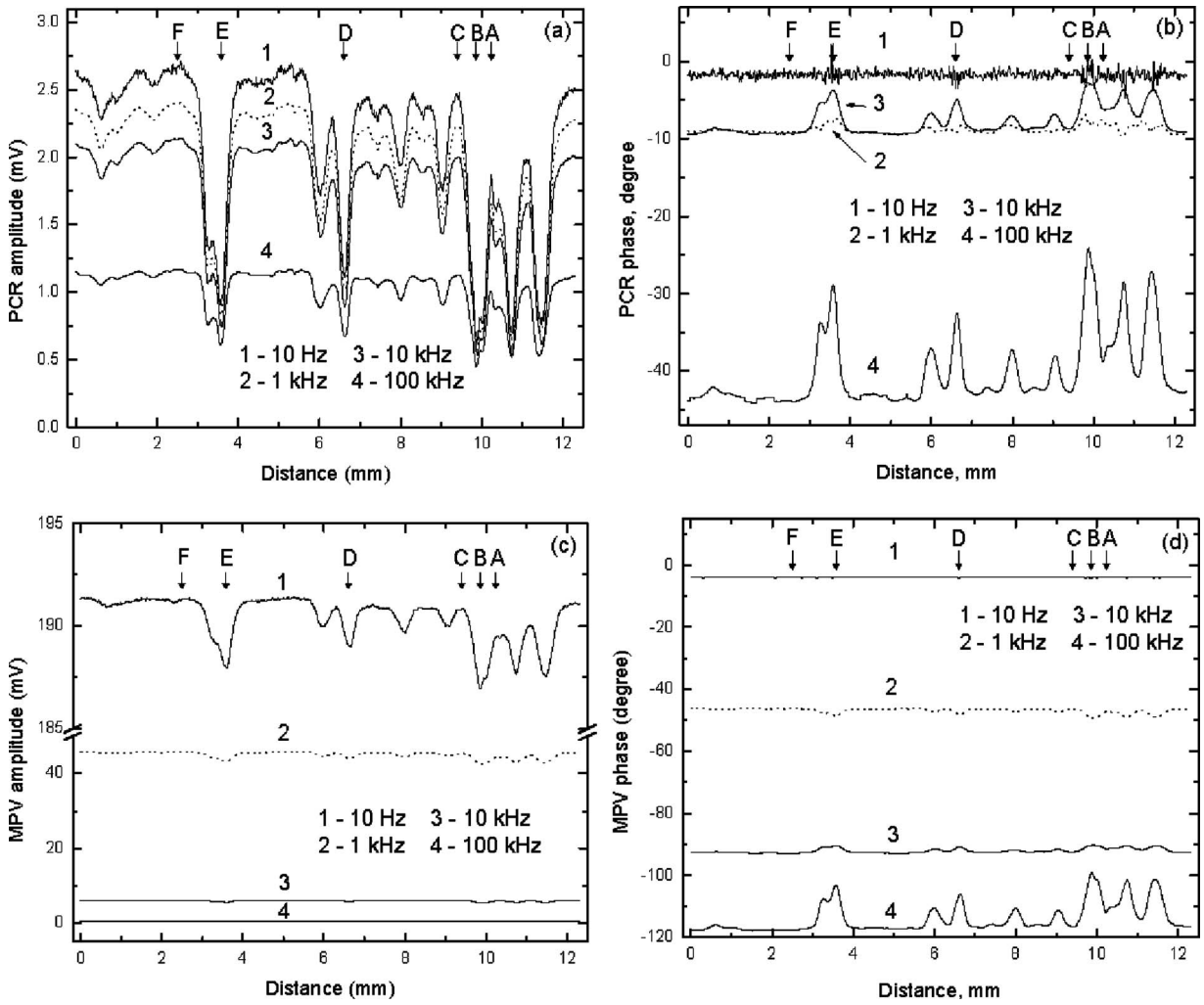

FIG. 9. Vertical point-by-point PCR and MPV line scans with step 20 μm along the dashed line in Fig. 6 at several frequencies. (a) PCR amplitude; (b) PCR phase; (c) MPV amplitude; and (d) MPV phase.

They are probably related to the different subsurface electronic transport paths probed by the two techniques.

By the same token, the overlap among the experimental curves of high-amplitude MPV, Fig. 7, at frequencies $f < 10$ kHz can be interpreted by the very small variation in the spatial distribution of the MPV, with the RC time constants remaining practically the same at the various locations across the solar cell, thereby indicating junction homogeneity. Nevertheless, the comparison between the PCR and MPV images points to a higher sensitivity to defects and recombination centers of the former technique, although the MPV inset amplitude and phase images in Fig. 7 show that adequate contrast exists and yields excellent correlation with that of the PCR images. However, in addition to the poorer contrast, MPV requires sequential point-by-point optical excitation to yield spatially resolved imaging, compared to the fast full-illumination PCR imaging by camera lock-in carrierography demonstrated in this work, at vastly shorter time-per-image requirements.

3. Photocarrier transport mechanisms of MPV and lock-in carrierographic imaging

In order to further investigate the correlation between MPV and PCR imaging, Fig. 9 shows PCR and MPV line scans at several frequencies made vertically along the dotted line in the inset of Fig. 6. The line scans clearly show the excellent degree of correlation across the solar cell in agreement with the images in Figs. 6 and 7, albeit with much lower contrast dynamic range for the MPV signals. The PCR amplitude dips and phase-lag peaks are the result of beam crossing nonradiative recombination-promoting grain boundaries which decrease the carrier-wave density (amplitude) and shift the PCR phase lag to smaller values, closer to the front surface due to enhanced recombination or trapping. In agreement with the phase images accompanying the carrierographic Figs. 2 and 5, the low-frequency PCR phase scans are less sensitive to those defects and grain boundaries, as deeper subsurface contributions to the carrier-wave integral in Eq. (1) tend to mask the effects of the near-surface recombination centers. The optimum contrast for amplitude occurs at frequencies at which the ac diffusion length is commensurate with the subsurface depth of the recombination center. On the other hand, the MPV amplitude signal shows measurable contrast only at low frequencies, whereas the phase contrast is best at the highest frequencies (here: 100 kHz). The reason for these MPV differences is the series resistance of the solar cell which further dampens the free photoexcited carrier density wave away from its generation location, while

Downloaded 24 Dec 2010 to 128.100.48.213. Redistribution subject to AIP license or copyright; see http://jap.aip.org/about/rights_and_permissions

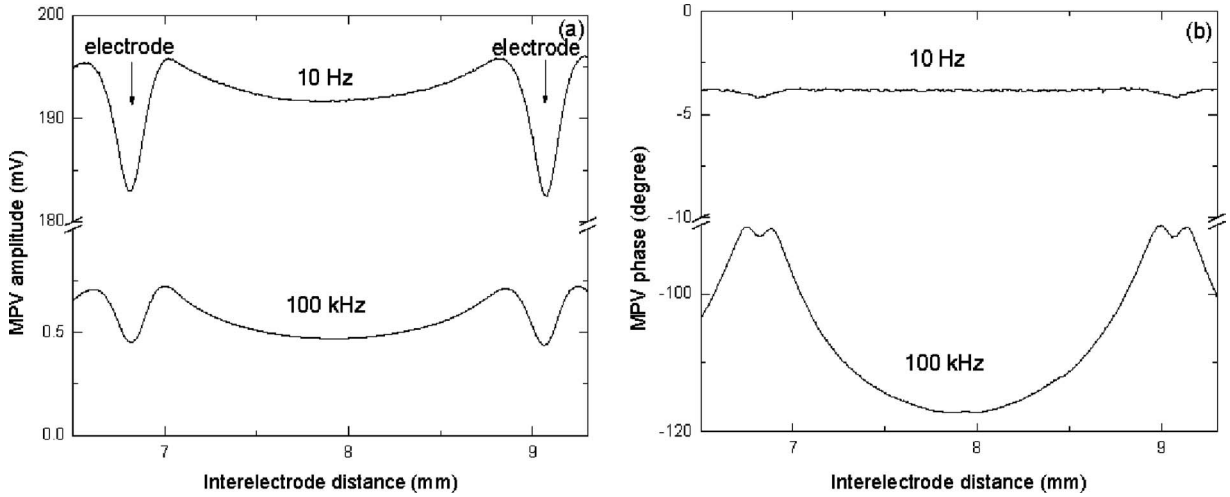

FIG. 10. Horizontal point-by-point MPV line scans with 20 μm step at several frequencies. (a) Amplitude and (b) phase.

diffusing toward the closest electrode for collection and conversion to photovoltage: the exponential spatial decay of the diffusing carrier wave with its characteristic ac diffusion length[19] effectively blocks carrier collection from generation distances longer than $L_e(\omega)$. For example, at locations along the line midway between electrodes the lowest frequencies (longest ac diffusion length) yield the highest signal and contrast (Fig. 10). All carriers arrive at the electrode for collection essentially IP with the modulated excitation source at 10 Hz, Figs. 7(b) and 9(d). Substantial phase-lag differences between recombination centers and intact optoelectronic source locations occur at much higher frequencies $f > 10$ kHz, Fig. 7(b), in agreement with Fig. 9(d). It is interesting to note the MPV phase reversal from lag to lead in the $f = 10$ and 100 kHz line scans, Fig. 9(d), at the various defect/grain boundary crossing regions. The low-frequency phase lags can be explained by carrier trapping in the rear-surface region, whence the deeper, underlying regions contribute the photocarriers dominating the MPV signal. These photocarriers can reach the closest electrode thanks to their long ac diffusion length at low frequency (lateral diffusion), however the MPV phase is lagged as they originate at subsurface locations farther away than those from the near-surface nondefective regions. Figure 9(d) shows evidence that high frequency MPV signals are dominated by laser detrapping of carriers trapped at defects and/or grain boundaries: given the short ac diffusion length at $f \geq 10$ kHz, the flux of detrapped free carriers generated closest to the neighboring electrode dominates the flux of the deeper-lying subsurface-generated free-carrier wave which is exponentially damped with distance from the electrode. As a result, the MPV phase from the defect/grain-boundary locations exhibits a lead over that from deeper intact locations with significant subsurface contributions to the electrode-collected free-carrier-density wave. This mechanism is also present in the PCR signal and laser detrapping contributes to phase lead at all frequencies, thereby establishing the stronger near-surface depth-profilometric character of the PCR depth-decaying carrier wave over MPV. In summary, highest MPV imaging contrast in mc solar cells can be obtained with low frequency amplitude (low spatial resolution) or with high frequency phase (high spatial resolution).

4. Subsurface optoelectronic defect sensitivity and depth-profilometric character of lock-in carrierography

In order to show the subsurface-defect-sensitive and depth profilometric character of the solar cell carrierographic image contrast, and link it to optoelectronic transport parameter changes induced by lattice damage to the substrate, Fig. 11 shows lock-in carrierographic amplitude images taken

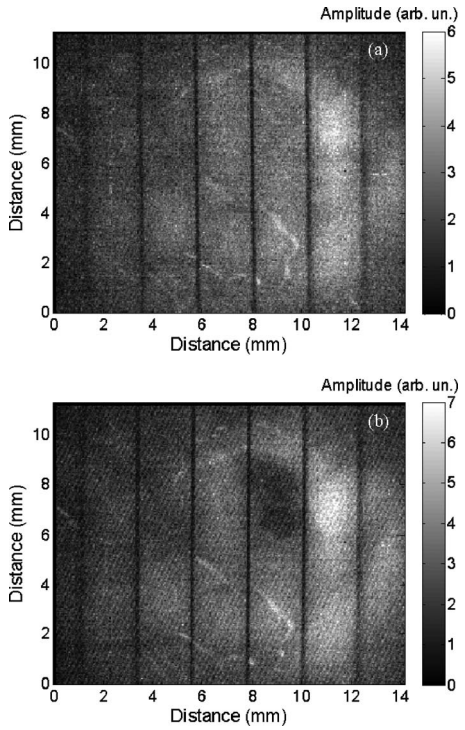

FIG. 11. Lock-in carrierographic amplitude images of a solar-cell fragment area at 10 Hz before (a) and after (b) mechanical damage to the back surface.

Downloaded 24 Dec 2010 to 128.100.48.213. Redistribution subject to AIP license or copyright; see http://jap.aip.org/about/rights_and_permissions

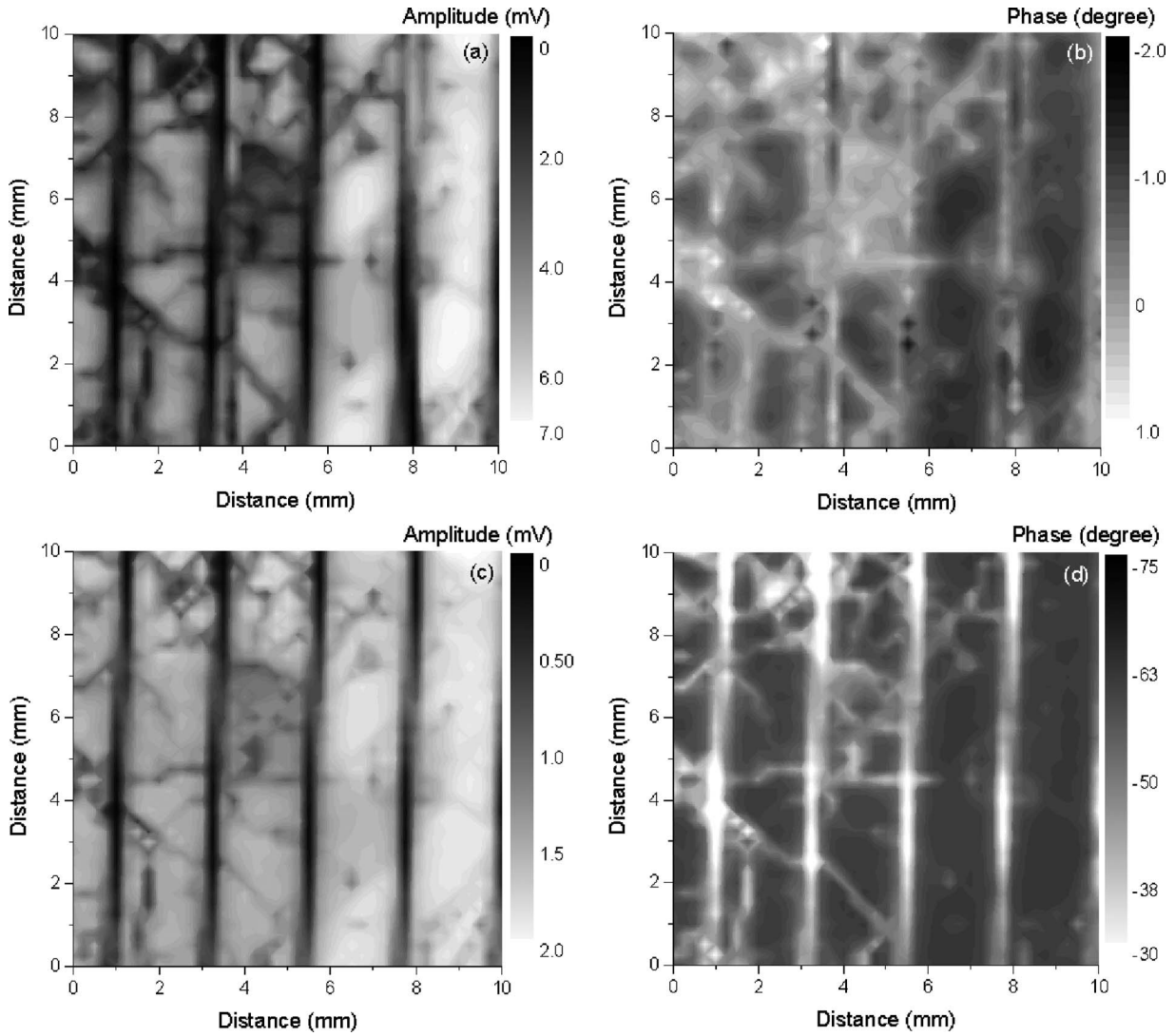

FIG. 12. Lock-in carrierographic amplitude and phase images of the back-surface damaged solar-cell fragment area of Fig. 11 at 1 kHz [(a) and (b)] and at 100 kHz [(c) and (d)].

with the expanded 532-nm laser from the front side of a mc solar-cell fragment before and after back-surface mechanical damage. In agreement with the Si substrate damage results of Fig. 2, the mechanical damage led to amplitude decrease at that location with a corresponding (much smaller) phase change (not shown here), creating contrast superposed on the mc grain-boundary structure of the solar cell. At higher frequencies, point-by-point PCR images of the same location were obtained through scanning with the focused 830-nm laser beam, Fig. 12. At 1 and 100 kHz, there is substantial phase contrast in both images. However, at 100 kHz the damaged area contrast has significantly decreased in both amplitude and phase images. This is consistent with the decreased ac diffusion length, Eq. (2), which diminishes contributions from back-surface recombination while improving resolution and contrast of near-front-surface regions where the majority of recombination centers is located. This type of carrierographic image quality is expected from improvements (increases) in the sampling rate of camera-based lock-in imaging.

IV. CONCLUSIONS

Lock-in carrierography (or PCR imaging) of multicrystalline silicon solar cells was introduced in two modalities: low frequency camera-based imaging and high-frequency point-by-point scan-based imaging. This novel technique was supplemented by, and compared with, MEL and MPV imaging. It was shown that contrast in NIR camera-based carrierographic images depends on the spatial integral of the free photoexcited carrier-wave density and thus is very sensitive to the grain-boundary and surface recombination-inducing structure of solar cells. Optimal contrast in both amplitude and phase images is obtained in the region of the knee of the frequency response curve. Imaging contrast and resolution is similar to that of MELI and superior to MPVI with the added advantage of the noncontacting nature of lock-in carrierography, thereby rendering this method suitable for fast optoelectronic quality control imaging at any and all stages of solar cell fabrication. The method allows for contactless control of spatially resolved transport parameters (lifetimes) of solar cells at operator-defined subsurface

Downloaded 24 Dec 2010 to 128.100.48.213. Redistribution subject to AIP license or copyright; see http://jap.aip.org/about/rights_and_permissions

depths (fixed modulation frequencies). The contrast physics of lock-in carrierography is controlled by the local characteristic lifetimes in the solar cell, namely the RC time constant of the *p-n* junction or the minority carrier recombination lifetime, depending on the modulation frequency at which imaging is obtained. It was shown that lock-in carrierography is very sensitive to subsurface electronic defects and can provide depth profilometric images with judicious adjustment of imaging frequency (camera frame rate). Comparison with MPV line scans revealed the possibility of laser detrapped photocarrier contribution to the PCR imaging, especially at high frequencies, $f > 10$ kHz. Comparison between camera-based and point-by-point scan-based imaging has shown that it is imperative to increase the sampling rate of commercial NIR InGaAs cameras for optimal optoelectronically sensitive amplitude and phase carrierography imaging of solar cells.

ACKNOWLEDGMENTS

The authors are grateful to Enfoton Solar, Kokkinotrimithia, Cyprus, for supplying the solar cells for this research. A. Mandelis acknowledges the support of the Canada Research Chairs (CRC) program and of the Natural Sciences and Engineering Research Council of Canada (NSERC) for a Discovery Grant.

[1]D. K. Schroder, *Semiconductor Material and Device Characterization* (Wiley, New York, 1998), Chap. 9; A. L. Fahrenbruch and R. H. Bube, *Fundamentals of Solar Energy Conversion* (Academic, New York, 1983), Chap. 7.
[2]M. D. Abbott, J. E. Cotter, F. W. Chen, T. Trupke, R. A. Bardos, and K. C. Fisher, J. Appl. Phys. **100**, 114514 (2006).
[3]J. Isenberg, S. Riepe, S. Glunz, and W. Warta, J. Appl. Phys. **93**, 4268 (2003).
[4]M. C. Schubert, S. Riepe, S. Bermejo, and W. Warta, J. Appl. Phys. **99**, 114908 (2006).
[5]T. Fuyuki, H. Kondo, T. Yamasaki, Y. Takahashi, and Y. Uraoka, Appl. Phys. Lett. **86**, 262108 (2005).
[6]T. Trupke, R. A. Bardos, M. C. Shubert, and W. Warta, Appl. Phys. Lett. **89**, 044107 (2006).
[7]P. Würfel, T. Trupke, T. Puzzer, E. Schäffer, W. Warta, and S. W. Glunz, J. Appl. Phys. **101**, 123110 (2007).
[8]D. Macdonald, J. Tan, and T. Trupke, Appl. Phys. Lett. **103**, 073710 (2008).
[9]T. Trupke, R. A. Bardos, M. D. Abbott, P. Wurfel, *et al.*, Proceedings of the 22nd European Photovoltaic Solar Energy Conference, Milan, Italy, 3–7 Sept. 2007, pp. 22–31; I. Tarasov, S. Ostapenko, K. Nakayashiki, and A. Rohatgi, Appl. Phys. Lett. **85**, 4346 (2004).
[10]M. B. Edwards, J. Bocking, M. D. Abbott, and J. E. Cotter, Proceedings of the 22nd European Photovoltaic Solar Energy Conference, Milan, Italy, 3–7 September 2007, pp. 1006–1010.
[11]A. Mandelis, J. Batista, and D. Shaughnessy, Phys. Rev. B **67**, 205208 (2003).
[12]A. Melnikov, A. Mandelis, J. Tolev, and E. Lioudakis, J. Phys.: Conf. Ser. **214**, 012111 (2010).
[13]D. Guidotti, J. S. Batchelder, J. A. Van Vechten, and A. Finkel, Appl. Phys. Lett. **48**, 68 (1986).
[14]D. Guidotti, J. S. Batchelder, A. Finkel, and J. A. Van Vechten, Phys. Rev. B **38**, 1569 (1988); D. Guidotti, J. S. Batchelder, A. Finkel, P. D. Gerber, and J. A. Van Vetchen, J. Appl. Phys. **66**, 2542 (1989).
[15]S. B. Zhang, S.-H. Wei, and A. Zunger, Physica B **273–274**, 976 (1999).
[16]J. Tolev, A. Mandelis, and M. Pawlak, J. Electrochem. Soc. **154**, H983 (2007).
[17]G. Busse, D. Wu, and W. Karpen, J. Appl. Phys. **71**, 3962 (1992).
[18]J. Batista, A. Mandelis, D. Shaughnessy, and B. Li, Appl. Phys. Lett. **85**, 1713 (2004).
[19]A. Mandelis, *Diffusion-Wave Fields: Mathematical Methods and Green Functions* (Springer, New York, 2001), Chap. 9.
[20]D. Shaughnessy and A. Mandelis, J. Electrochem. Soc. **153**, G283 (2006).
[21]A. Melnikov, A. Mandelis, J. Tolev, J. Xia, and E. Lioudakis, "Nondestructive infrared optoelectronic lock-in carrierography of mc-Si solar cells," QIRT J. (submitted).
[22]A. Mandelis, J. Appl. Phys. **66**, 5572 (1989).
[23]S.-Y. Zhang and J.-C. Cheng, Semicond. Sci. Technol. **6**, 670 (1991).
[24]C. Munakata, N. Honma, and H. Itoh, Jpn. J. Appl. Phys., Part 2 **22**, L103 (1983).
[25]N. Honma, C. Munakata, H. Itoh, and T. Warabisako, Jpn. J. Appl. Phys., Part 1 **25**, 743 (1986).

Downloaded 24 Dec 2010 to 128.100.48.213. Redistribution subject to AIP license or copyright; see http://jap.aip.org/about/rights_and_permissions